Mechanical properties of C 60 at finite temperature from first-principles calculations

Laurent Pizzagalli

Mechanical properties of C_{60} at finite temperature from first-principles calculations

L. Pizzagalli[a,*]

[a]*Institut P', CNRS UPR 3346, Université de Poitiers, SP2MI, Boulevard Marie et Pierre Curie, TSA 41123, 86073 Poitiers Cedex 9, France*

Abstract

C_{60} has been the focus of many studies since its discovery, but the mechanical properties of this unique molecule remain poorly known. To remedy that, we performed density functional theory molecular dynamics calculations of the compression of C_{60} at finite temperature, within a large strain range. The possible recovery of the molecule after unloading was also investigated with first principles accuracy, for two different modes. We found that the behavior of C_{60} follows three regimes depending on the compression strain. Up to 0.48 ± 0.02, the deformation is elastic with a small but distinct influence of the compression orientation. A relation between the electronic gap and the orientation is also revealed. The second regime starts for larger strains up to 0.75 ± 0.02, after a 30–32 nN force plateau. It is characterized by stochastic carbon bond breakings. Although bonds rupture is generally the fingerprint of plastic deformation in materials, we found that the C_{60} structure can be dynamically recovered in a significant fraction of cases, following a fast unloading. This mode also yields defected structures with low energies compared to a slow unloading mode. Finally, the third regime corresponds to irreversible deformation of the molecule, for strains larger than 0.75 ± 0.02.

Keywords: mechanical properties, buckminsterfullerene C_{60}, first-principles molecular dynamics calculations

1. Introduction

The buckminsterfullerene C_{60} belongs to the class of the most famous and studied molecules, partly due to its recognizable shape and its pioneering role in the emergence of other fullerenes like the carbon nanotubes. Since its identification in 1985, countless studies were conducted to discover and understand its characteristics. These efforts bore fruit as we have now at disposal a wealth of information for various of its properties in chemistry, electronics, optics, etc... [1, 2].

In contrast, the mechanical properties of C_{60} remain poorly understood. The most prominent result concerns its extraordinary resilience i.e., the ability of C_{60} to recover its initial shape after being severely compressed as a consequence of high energy impacts on surfaces [3–6]. These pioneering studies were supplemented by a few theoretical and numerical investigations of the elastic properties of C_{60}. The bulk modulus is determined to be in the range 710–860 GPa [7, 8], surprisingly much higher than a predicted value of 2 GPa for the Young modulus [9]. A few researchers performed molecular dynamics calculations of the molecule compressed between graphene layers [10, 11]. Unfortunately these works do not allow for quantifying intrinsic mechanical properties of C_{60} like the yield stress and the elastic limit, because of the presence of the deformed graphene layers. More recently, Shen reported the calculated variation of the compression load as a function of strain [12]. This work raises questions because surprisingly large maximum force and stiffness were predicted, which may be related to the compression method.

In brief, only conflicting and limited information is available concerning the mechanical properties of C_{60}. This is in contrast to carbon nanotubes for which both elastic and plastic behaviors have been thoroughly investigated [13, 14]. Improving beyond the current state of knowledge is important for fundamental research, and would certainly be beneficial for a better understanding of the mechanical properties of aggregated or polymerized C_{60}-based materials [15–18].

Recently, a method allowing for the first principle modeling of nanoparticle compression was proposed, and its feasibility demonstrated in the case of C_{60} [19]. It is demonstrated in this work that the C_{60} shell begins to yield for a compression strain close to 0.5, which contradicts the earliest studies using classical interatomic potentials where a much larger strain was predicted. However important aspects were left unexplored, such as the identification of the mechanical transition occurring at this strain or the influence of temperature. To fill the gap of knowledge we have performed a large number of simulations of the compression and unloading of a C_{60} molecule in various conditions. They allowed us to determine with an unprecedented accuracy the mechanical properties of this molecule. In particular, three distincts regimes are identified depending on the compression strain. For low and high strain values the deformation is elastic or plastic,

*Corresponding author: Tel: +33 549497499. E-mail: Laurent.Pizzagalli@univ-poitiers.fr

respectively. However, for medium strain values, we show that carbon bond breakings occurring during compression can be partially or even fully healed during unloading, especially by a dynamical recovery process. These findings are reported in the present paper. Calculations are first detailled in section 2, followed by a descrption of all results in section 3. The next two sections are a discussion of these results, and a conclusion.

2. Computational details

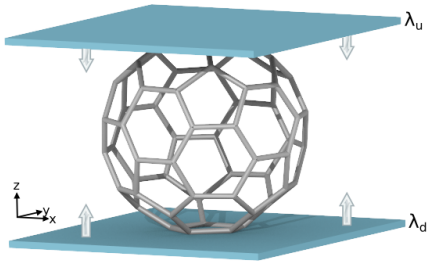

Figure 1: Compression of the C_{60} molecule between two planar repulsion force fields (represented by the thin turquoise slabs), located at z-coordinates λ_u and λ_d, and moving towards each other.

Compression and slow unloading simulations were performed following the method described in Ref. [19]. For each run, two parallel planes were initially defined on either side and at equal distance of the C_{60} molecule, along the z-axis (Fig. 1). The planes positions λ_u and λ_d were decreased and increased, respectively, at each iteration during a compression simulation (and the opposite during unloading). For all atoms whose z-coordinates were greater (lower) than λ_u (λ_d), an additional compression force proportional to a constant K and to the square of the difference between the z-coordinate and λ_u (λ_d), orientated along the z-axis and towards the center of the molecule, was applied (Fig. 1). This procedure allows for a gradual and smooth compression of the molecule, and has been largely used for classical molecular dynamics simulation [20–24]. The originality of the present approach lies in the combination of these planar repulsion force fields with first principles molecular dynamics [19].

The electronic structure was calculated in the framework of density functional theory [25, 26], with a plane waves cutoff of 25 Ry for representing the wavefunctions. The Quantum Espresso suite [27] was used. The exchange-correlation contributions were computed using the PBE functional [28]. Ultrasoft pseudopotentials [29] were employed to describe electron-ion interactions. The C_{60} molecule was located in a $(20\ \text{Å})^3$ supercell, which is large enough to prevent artificial interactions between replicas [30]. A conjugate gradient energy minimization led to bond lengths equal to 1.401 Å and 1.451 Å, in excellent agreement with the literature [31].

The Car-Parrinello molecular dynamics scheme was used for compression and slow unloading simulations, with a timestep equal to 0.2 fs. The effective electron mass and the electron mass cutoff were set to 600 a.u. and 5 Ry, respectively [32]. Nose-Hoover thermostats were used for both electronic and ionic degrees of freedom, with an electronic kinetic energy target of 0.005 a.u. and an oscillation frequency of 90 THz for electrons, and a temperature target of 300 K and an oscillation frequency of 30 THz for the ions. Supplementary calculations at a ionic temperature of 1 K and an electronic kinetic energy target of 1.66×10^{-5} a.u. were also carried out. The two planar repulsion force fields moved at a velocity of 0.05 Å/ps, yielding compression/unloading speeds of 0.1 Å/ps. The repulsion strength was set to 30 a.u. Finally, friction forces were applied on atoms already subject to compression forces, in order to prevent an excessive and steady rotation of C_{60} during compression/unloading [19]. Friction coefficients Γ equal to 50 and 500 a.u. were used in this work. The first value allows for slight and occasional rotations of C_{60} with respect to the compression axis. On the contrary, using the second value nearly suppresses rotations. A typical compression run lasted 272000 iterations, which corresponds to a maximum deformation of about 80%. Two different C_{60} orientations were investigated, with the compression axis passing either through an hexagon center (noted H in the following), or through a pentagon center (noted P).

Additional molecular dynamics calculations with no external forces were carried out with compressed molecules as initial configurations, to simulate a fast unloading. These calculations were performed using Born-Oppenheimer molecular dynamics with a timestep equal to 0.484 fs. In fact, the use of Car-Parrinello molecular dynamics was found to be inappropriate in that case because of the large temperatures generated by the fast release of mechanical energy. In these simulations, 1000 iterations with no thermal constraints were first carried out, followed by 1000 iterations with a Berendsen ionic thermostat set at 300 K.

Finally, nudged elastic band (NEB) calculations [33] were also performed to determine the activation energy associated with a carbon bond breaking under compression. These simulations included seven replicas, five being optimized using a quick-min algorithm. In order to preserve the strained state of C_{60} in NEB calculations, topmost and bottommost carbon atoms were not allowed to move along the z-axis direction. These atoms were identified as being in contact to a planar repulsive force field during the compression stage. The NEB force convergence threshold was set to 0.05 eV Å^{-1}, and the spring constants to 0.04 hartrees. Two calculations were carried out in succession, using the climbing image method [34] in the second one to determine the activation energy with high precision.

Several properties characterizing the atomic and electronic structures of the molecule were monitored during simulations. The potential energy is a direct outcome of DFT calculations. It is expressed relatively to the potential energy of a free C_{60} molecule at 300 K (or at 1 K),

which is obtained by an independent molecular dynamics calculation. These calculations were also used to determine the initial dimension d_0 of C_{60} along the compression axis. The displacement during the compression/unloading is calculated as $\delta = d_0 - d$, with $d = \lambda_u - \lambda_d$, and the engineering strain as $\varepsilon = \delta/d_0$. At last, the contact force during compression/unloading is given by summing the external compression forces due to one planar repulsion force field. Practically, it is calculated as the average of the two contact forces associated with upper and lower force fields.

3. Results

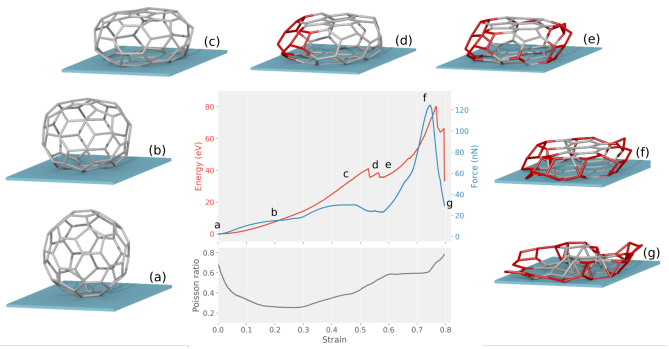

Figure 2: Energy (red line), contact force (blue line), and Poisson ratio (black line) as a function of compression strain for a P orientation ($\Gamma = 500$ a.u.). Curves are smoothed by performing rolling averages with a strain period of 0.00294 for the energy, of 0.0294 for the contact force, and 0.0588 for the Poisson coefficient. (a)-(g) pictures showing the configurations obtained at different strains: 0 (a), 0.20 (b), 0.45 (c), 0.55 (d), 0.60 (e), 0.735 (f), 0.795 (g). The turquoise thin slab symbolizes the bottom repulsive force field (The upper one was removed for a clearer picture compared to Fig. 1). Bonds between carbon atoms are drawn up to a separation of 1.81 Å. Grey bonds correspond to a local graphene-like atomic arrangement, as determined using the polyhedral template matching method and a root-mean-square deviation cutoff of 0.35 [35]. Unidentified local geometries with this method, typically due to broken bonds and local reconstructions, are shown with red bonds.

A typical outcome of a simulation is presented in Fig. 2 (an extensive set of energy and force curves is shown in Fig. S1–S4 in Supplementary Material). During the first steps, the compression of the two caps in contact with the top and bottom repulsion force fields is observed (Fig. 2-(a-b)). This C_{60} flattening occurs with little lateral expansion as evidenced by the decrease of Poisson ratio up to a strain of about 0.3 ((Fig. 2). This initial stage is characterized by quadratic and linear increases of the potential energy and contact force, as expected for an elastic deformation. Note that non-linear contributions become clearly visible for strains greater than about 0.1, with the contact force seemingly reaching a plateau. At strains close to 0.3, a positive inflection can be seen for both energy and force curves. It is correlated with an increase of contact surfaces and the beginning of the lateral expansion of C_{60} (Fig. 2-(b-c)), as evidenced by the augmentation of the Poisson ratio. The contact force saturates at strains greater than about 0.4, to reach a plateau defined by a value equal to 30–32 nN.

The contact force markedly decreases at strains greater than 0.47–0.49. In this stage, atomic bonds in the equatorial region of the compressed molecule are so severely stretched that one or two carbon bond break. This is usually followed by local reconstructions of the atomic structure, visible in the energy curve as sharp drops (Fig. 2-(d-e)). Such events occurred in all compression runs, for strains ranging between 0.50 and 0.70 approximately. Furthermore, for strains greater than 0.6, the slopes of both the energy and the contact force increase significantly. At large deformations the molecule resembles two flat carbon layers connected by bonds at their edges (Fig. 2-(e-f)). For strains equal to about 0.75–0.77, maximum energy and contact forces, close to 80 eV and 120 nN respectively, are reached. Ultimately the C_{60} shell mechanically fails by the breaking of several bonds over a short strain interval (Fig. 2-(g)). A movie showing the whole sequence in relation with energy and force variations is available in the Supplemental Material.

3.1. Low strains

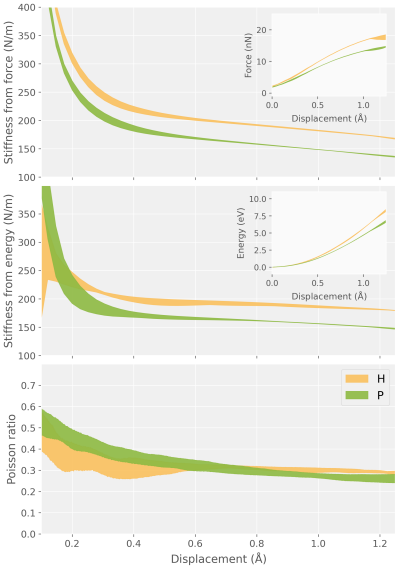

Figure 3: Stiffness and Poisson ratio of C_{60} as a function of displacement, during compression at 300 K. The yellow and green colors correspond to simulations with H and P orientations, respectively. The widths of the plots display the variations associated with several runs. Top: stiffness determined by an affine fit of the contact force (represented in the inset plot). Middle: stiffness determined by a quadratic fit of the C_{60} potential energy (shown in the inset plot). Bottom: Poisson ratio.

As mentioned above, both energy and contact force variations at low strains are in agreement with a linear elastic regime. The mechanical stiffness k can then be rigorously determined as the slope of the force-displacement curve ($F = k\delta$), or as twice the quadratic coefficient of the energy-displacement curve ($E = k\delta^2/2$). Figure 3 shows

the values calculated from all runs at 300 K, as a function of the displacement range used in the energy or force fit. For displacements lower than about 0.4 Å, accurate fitting is difficult because of the small size of the molecule and thermal vibrations, which leads to large and strongly decreasing stiffness values. The slopes of stiffness curves are significantly reduced but not completely canceled, by using larger displacements. This suggests that the elastic deformation is not perfectly linear. Note that similar trends and values are obtained from compression simulations carried out at 1 K (not shown).

Figure 3 clearly indicates that the stiffness depends on the compression orientation. In fact, values ranging from 220 N m^{-1} to 180 N m^{-1} are computed for H, and from 185 N m^{-1} to 150 N m^{-1} for P. The difference is approximately 30 N m^{-1} for a large displacement range and from both energy and force fits. This compares extremely well with first-principles static calculations yielding a difference of 33 N m^{-1} between both orientations [36]. Furthermore, Pawlak et al. previously reported that the C_{60} stiffness depends on the position of the AFM tip apex used to press down on the molecule [37], in qualitative agreement with our work. Unfortunately, a direct quantitative comparison with their measurements is not possible since the loading processes are different.

Figure 3 also shows the Poisson ratio calculated for an increasing displacement range, in the elastic domain. As with stiffness, it is difficult to extract accurate values for displacements lower than 0.4 Å. Increasing the displacement range leads to a Poisson ratio close to 0.3 for both H and P i.e., with no clear dependence on the orientation. At 1 K however, different Poisson ratio values are calculated, with 0.31 for H and a value ranging from 0.21 to 0.24 for P. The reason for such a difference between 300 K and 1 K simulations is not straightforward. Note that a comparison with the literature is not possible since there are no published values to our knowledge.

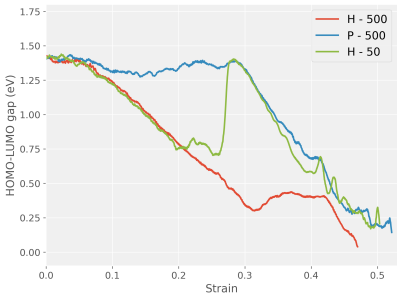

Figure 4: HOMO-LUMO gap of C_{60} as a function of compression strain, for three simulations: strong friction (Γ = 500 a.u.) with either H (red curve) or P (blue curve) orientations, and weak friction (Γ = 50 a.u.) with H orientation (green curve).

An interesting phenomenon is observed for runs with an initial H orientation and a low friction coefficient Γ = 50 a.u. For strains greater than about 0.2, small C_{60} rotations are observed which change the C_{60} orientation from H to P. This process typically takes place in two steps, with an intermediate state defined by the compression axis centered at the boundary between an hexagon and a pentagon. This reorientation process is in agreement with the lowest elastic energy and contact force for the P orientation (Fig. 3). It suggests that the reorientation with respect to the compression might be possible in the case of a physisorbed C_{60}. By increasing the friction coefficient to 500 a.u., rotations are hindered and the initial H orientation can be preserved. Interestingly it is possible to detect the orientation change of C_{60} by monitoring the variations of the HOMO-LUMO gap of the molecule during compression, shown in Fig. 4 for three different cases. The gap decreases for strains greater than 0.06, but while a large and seemingly linear reduction is obtained for the two H runs, only a weak decrease followed by a slow recovery is predicted for P. For the H run with a low friction coefficient, the HOMO-LUMO gap stops to decrease at a strain of about 0.2 and, after some fluctuations, sharply increases to reach the same value than for the P run. This behavior is obviously correlated with the reorientation of C_{60} in this strain range. A maximum difference of almost 1 eV is predicted between both orientations. This would suggest that it might be possible to identify the compression axis with respect to the C_{60} structure by measuring the HOMO-LUMO gap. Finally, for strains larger than 0.3, which corresponds to the beginning of C_{60} lateral expansion, the HOMO-LUMO gap decreases for the P-oriented compression, whereas for the H case it first increases, saturates, then decreases towards zero. The C_{60} gap closure under compression has already been reported in the literature [38]. We further predict that the gap decrease rate and the threshold strains both depend on the compression orientation.

3.2. Large strains

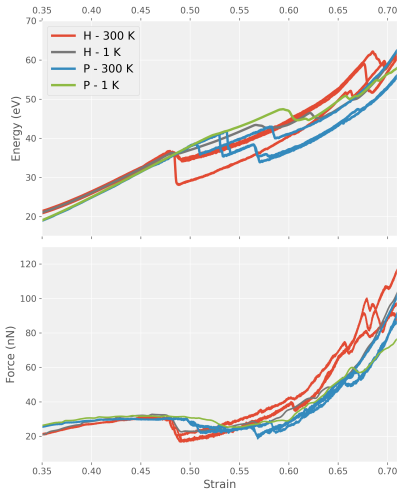

Figure 5: Energy and contact force as a function of strain for different conditions: H orientation at 300 K (red lines) and at 1 K (black line), P orientation at 300 K (blue lines) and at 1 K (green line). Selected runs were all performed with a friction coefficient $\Gamma = 500$ a.u., in order to preserve the initial orientation during all the compression test. Three independent simulations were performed at 300 K to reveal the stochastic nature of the energy drops observed for strains greater than 0.48.

For strains greater than about 0.40, the contact force first experiences a plateau with a value of 30–32 nN, although the energy continues to increase (Fig. 2). This plateau is observed in all investigated cases i.e., independently of the orientation or the temperature, as can be seen in Fig. 5. It ends abruptly at a strain of 0.47–0.48 for the H orientation, and more smoothly for the P orientation at slightly higher strains of 0.49–0.50. Note that this approximate 0.02 strain difference between H and P cases is maybe not significant because of the aforementioned uncertainty in the definition of the zero strain. The presence of a similar force plateau was observed in indentation experiments on a C_{60} molecules island [39], albeit at a lower value of about 20 nN. However, our results disagree with previous theoretical studies. In fact, Shen reports a similar plateau but at a surprisingly high value of about 1100 nN from approximate quantum mechanical calculations [12]. Furthermore, classical interatomic potential simulations lead to a contact force maximum of 20 nN for similar strains, except that no plateau is obtained [40].

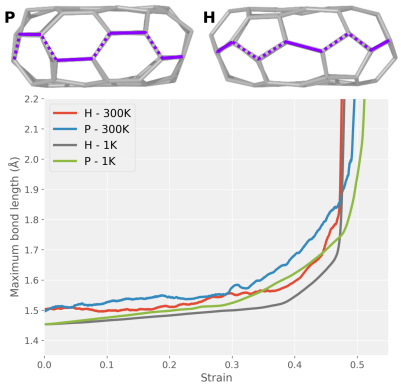

Figure 6: Maximum C–C bond length as a function of strain for different conditions: H orientation at 300 K (red line) and at 1 K (black line), P orientation at 300 K (blue line) and at 1 K (green line). The top pictures show the H and P configuration at a 0.47 compression strain, with 'equatorial' bonds highlighted in violet. Solid lines indicate bonds which are observed to break during compression.

The contact force decreases for strains greater than 0.47–0.50, due to the breaking of one or more C–C bonds in the equatorial region of the C_{60} shell. This is demonstrated in Fig. 6 which shows the variation of the maximum C–C bond length for several cases. For a P orientation, one can observe a first inflection at a strain close to 0.3 corresponding to the beginning of the lateral expansion of C_{60} (Fig. 2). A second inflection point occurs at a strains 0.48-0.50, the almost vertical increase revealing the breaking of a bond. The structures analysis shows that the C_{60} shell exhibits an armchair configuration for a P orientation (Fig. 6). C–C bonds that break are perpendicular to the compression axis, allowing for a maximum stretching, and form the edges between hexagons and pentagons. For systems with an H orientation, inflection points occur first at about 0.38, and then at 0.48 (Fig. 6). They are characterized by a zigzag configuration along the compression axis (Fig. 6), and the bonds breaking first form the edges between two hexagons. Inflection points occur first at about 0.38, and next at 0.48 (Fig. 6).

Note that it is always the same kind of C–C bond which breaks first for either H or P orientations. However this initial event triggers diverse structural modifications of the C_{60} molecule, often involving partial reconstruction in the vicinity of the broken bond. These reconstructions events correspond to well defined drops on energy curves, occurring immediately after the first bond breaking or at somewhat larger strains (Fig. 5). Reconstruction mechanisms involving the most atoms are typically associated with the largest energy drops. On the contrary, some light structural changes are unnoticeable from energy variations only, because the energy release is more than compensated by the elastic energy increase during the ongoing compression. It is the case for the first bond breaking event in P configurations for instance.

Various C_{60} configurations are then obtained, with one or two shell openings which could be weakly or largely reconstructed (see fig. 2-(d-e), and Figs. S1–S4 in Supple-

mentary Material). No clear correlation is found between the structural change or its associated energy drop, and the strain at which it occurs. Furthermore, reproducibility is only achieved for 1 K simulations. All these factors clearly demonstrate the stochastic character of the reconstruction mechanisms following the initial bond breaking event.

The last salient characteristics of the compression curves are the high force and energy maxima reached at large strains, followed by significant drops due to the total flattening of the C_{60} shell. These maxima occur in a strain range 0.74–0.78 for the energy, and 0.73–0.76 for the contact force, depending on cases. On averages, the maximum energy and force before the drops are 83 eV and 126 nN, with extreme values as high as 96 eV and 150 nN, respectively. However, these numbers should be considered with caution, especially for the force, since they depend on the averaging procedure used to smooth fluctuations.

3.3. Unloading

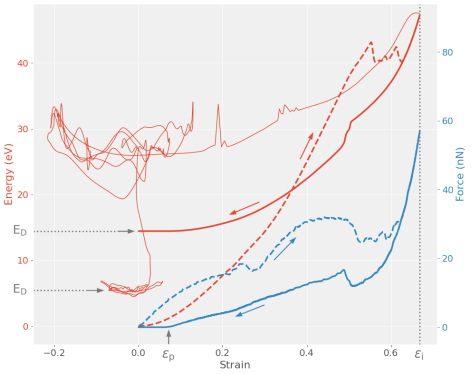

Figure 7: Energy (red lines) and contact force (blue lines) as a function of strain during the compression/unloading of a C_{60} molecule (P, $\Gamma = 50$ a.u., 1 K). The zero energy reference corresponds to the initial perfect C_{60} molecule. Dashed lines correspond to the compression stage, whereas thick full lines correspond to unloading obtained by slowly moving off the two planar repulsion force fields (S unloading), starting at a strain $\varepsilon_i = 0.668$. The residual plastic strain ε_p is determined when the contact force reaches zero during unloading. Also shown in the figure is the energy variation (thin red line) resulting from the unconstrained evolution of the molecule (F unloading). For both S and F unloading modes, we define the defect energy E_D as the energy difference between the final configuration and the perfect C_{60}.

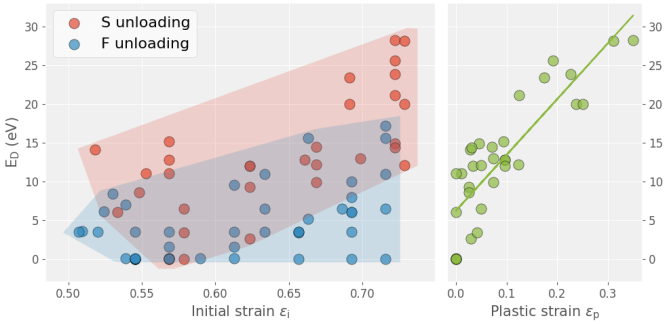

Figure 8: Left: Defect energy E_D as a function of the initial compression strain ε_i for several configurations. The red (blue) dots correspond to S (F) unloading simulations, respectively. Right: Defect energy E_D versus the final strain ε_p in S unloading simulations (green dots). The green line is the result of a linear regression fit.

In this section, the results of unloading simulations are described. Several configurations are first selected in various runs and at different compression strains ε_i. For each of them, a molecular dynamics simulation is performed using the same conditions than for the compression, but now moving off the two planar repulsive planes. These simulations are referred to as slow (S) unloading in the following. Figure 7 shows an example of computed energy and contact force during a loading-unloading cycle. Compression and unloading curves are similar at first and begin to diverge at an approximate strain of 0.625, which corresponds to a bond breaking and reconstruction event. Energy and contact force curves in the unloading regime are typical of an elastic behavior, except for the sharp decrease (increase) in energy (force) at a strain of 0.506, suggesting structural reconstructions. We define the residual plastic strain ε_p as the strain at which the contact force reaches zero during the unloading stage (alternatively the potential energy becomes constant). Another interesting quantity is the final energy E_D at the end of the unloading stage, called defect energy in the following. Both ε_p and E_D are equal to zero when a perfect C_{60} molecule is recovered after unloading. We tested a different unloading mode (F) where the C_{60} molecule is relaxed with no planar repulsive fields, first with no temperature control then with a 300 K thermostat. The energy–strain relation is represented in Fig. 7. The two temperature regimes are clearly visible, with large strain fluctuations and a high energy in the first one, followed by a significant potential energy reduction in the second one. E_D is obtained by averaging the energy in the second regime.

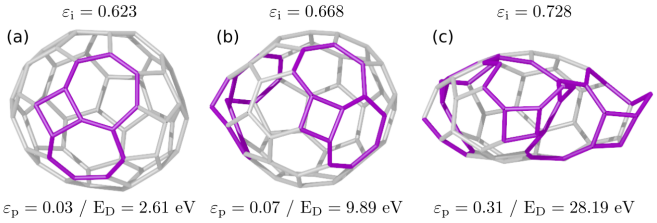

Figure 9: Final geometries obtained after three independent S unloading calculations. The initial configurations are obtained from a compression simulation with a P orientation (Γ = 50 a.u., 300 K), at strains ε_i equal to 0.623 (a), 0.668 (b), and 0.728 (c). Bonds between carbon atoms are drawn for a maximum separation of 1.81 Å. Structural defects are marked with violet bonds.

S unloading simulations were carried out for initial configurations corresponding to strains ε_i ranging from 0.50 to 0.74, at which one or several bond breaking mechanisms occurred. Calculated defect energies E_D and plastic strains ε_p are reported in Fig 8. Overall, high E_D and ε_p values appear to be correlated with large initial strains. Our data also suggest an approximate linear relation between E_D and ε_p (Fig. 8). A first domain can be roughly defined for $\varepsilon_i \lesssim 0.65$, which corresponds to initial structures where the C_{60} shell is opened at one place in most cases, with a moderate reconstruction (see Fig. S1-S4 in supplementary materials for examples). In that case S unloading calculations yield final configurations with E_D <15 eV and ε_p <0.1. The elastic energy is largely relaxed, but structural defects are not or imperfectly cured during unloading. Those are shell openings or local modifications of the normal pentagon-hexagon patterning (Fig. 9-(a)). Only 4 among 33 simulations allow for retrieving the perfect C_{60} structure ($E_D = 0$, $\varepsilon_p = 0$). In these runs the initial structures (shown in Fig. S1-(a,c) and Fig. S2-(d)) include two or three broken bonds with no local reconstructions, which can be reformed straightforwardly during the unloading. It suggests that remaining defects after unloading are a consequence of the bond reconstruction events occurring during compression.

For initial strains $\varepsilon_i \gtrsim 0.65$, we find that E_D ranges from 10 eV to at most 28 eV whereas ε_p ranges from 0.03 to 0.35 (Fig 8). The pristine C_{60} molecule is then never recovered, and a significant part of the mechanically stored energy is not relaxed during unloading (see two examples in Fig. 9-(b,c)). In fact the initial structures are heavily distorted with several reconstructed bonds, which can hardly be recovered during unloading.

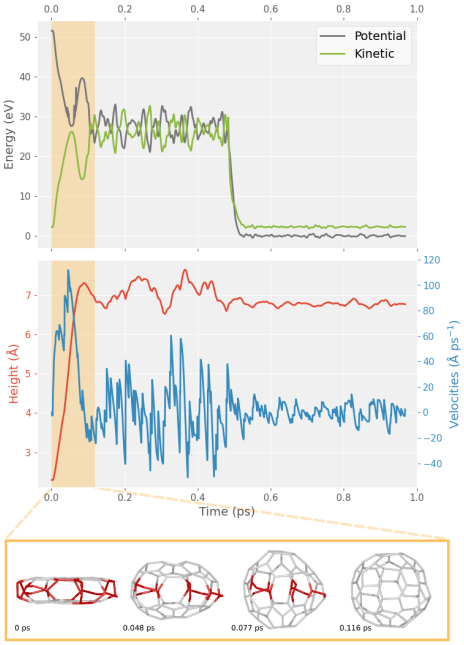

Figure 10: Top: potential (black) and kinetic (green) energies as a function of the MD time (ps) during a F unloading simulation (1000 iterations i.e., 0.484 ps in a NVE ensemble, followed by 1000 iterations with a 300 K ionic thermostat). The potential energy reference is equal to -10103.003 eV, which is the average potential energy of a perfect C_{60} at 300 K in our simulations. The initial configuration corresponds to a compression strain of 0.67. Middle: C_{60} height (red) and height velocity (blue), for the same simulation. The C_{60} height is determined at each iteration as the difference between the maximum atomic separation along the axis used for compression. The height velocity is calculated as the derivative of the C_{60} height with respect to the MD time. Bottom: Selected snapshots from the MD simulation at selected times in the range [0 – 0.116] ps (yellow frame).

We now focus on the results of F unloading simulations. An example of the variations of quantities monitored during a Born-Oppenheimer molecular dynamics calculation is shown in Fig. 10, together with snapshots of the C_{60} structure at selected times. At startup, the potential energy of the deformed C_{60} molecule is equal to 51.7 eV, and the kinetic energy to $3Nk_BT/2 = 2.33$ eV with $T = 300$ K. A fast expansion with an increasing speed is observed during the following steps, similar to a spring release along the compression direction. The C_{60} shell extremities reaches a maximal speed of 112 Å ps^{-1} at 0.046 ps, and a height equal to 7.3 Å at 0.108 ps. The release process appears to be already completed at 0.11 ps with both kinetic and potential energies oscillating between an average value of 27 eV, in agreement with the equipartition theorem. Although the vibrational mode Hg(1) corresponding to the longitudinal vibration along the compression axis [41] remains dominant, other phonon modes become populated during the following iterations. Assuming all kinetic energy could be equated to a thermal energy, an average temperature of 3480 K is determined (Fig. 10). After 1000 iterations i.e. 0.484 ps, a 300 K thermostat is applied and the potential energy becomes negligible, suggesting that a

perfect C_{60} molecule is recovered. A movie showing the C_{60} evolution is available in the Supplementary Material.

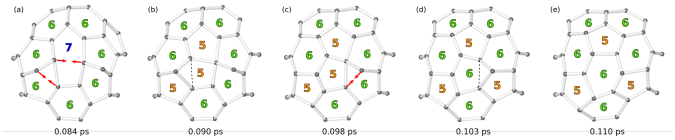

Figure 11: (a-e) Example of a reconstruction mechanism of the C_{60} shell occurring during a F release simulation. Only a part of the shell is shown for clarity. The colored digits indicate how many C atoms belong to each ring (blue for heptagons, green for hexagons, orange for pentagons). The red arrows show how new bonds will form, whereas dashed black lines show where bonds disappeared.

A structural analysis indeed confirms that all initially present topological defects disappeared in this simulation, and that healing occurred in a very short timespan between 0.077 ps and 0.11 ps (Fig. 8). A reconstruction mechanism is illustrated in Fig. 11 for the same system. The initial configuration includes an heptagon encircled by hexagons at 0.084 ps (Fig. 11-(a)). Two new bonds are concurrently created while one is broken, leading to the formation of three adjacent pentagons at 0.09 ps (Fig. 11-(b)). The central pentagon is next transformed into an hexagon by a bond-switching mechanism between 0.098 ps and 0.103 ps (Fig. 11-(c-d)). The regular alternating hexagon-pentagon pattern is finally recovered (Fig. 11-(c-d)).

A perfect C_{60} geometry (i.e. $E_D = 0$ eV) is recovered in one third of the 45 performed F unloading simulations i.e., in a significantly higher proportion than in S unloading calculations. It occurred more frequently for initial configurations with strains ranging from 0.50 to 0.65, but also for three cases with larger strain values (Fig. 8). Another interesting result is the overall lower defect energies for F unloading compared to S unloading simulations (Fig. 8). In fact, for F unloading, E_D is always lower than 17.2 eV (72% of the S simulations). This can be explained by less topological or coordination defects left after F unloading. Furthermore, 62% of the runs lead to E_D lower than 5 eV, to be compared to only 18% for S unloading. Such small E_D values are typically associated with only one topological defect, as seen in Fig. 9-(a).

4. Discussion

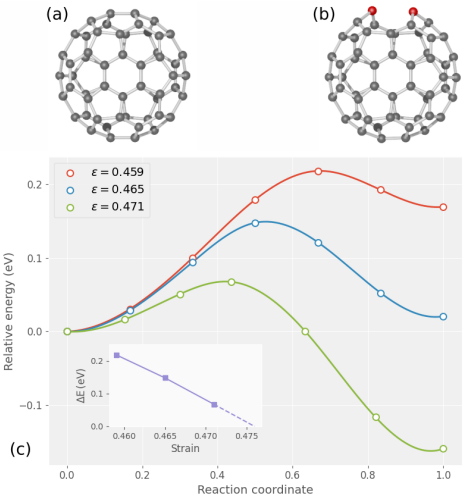

Figure 12: Initial (a) and final (b) atomic configurations (top view) used in nudged elastic band calculations. Carbon atoms with coordination 3 (2) are shown as black (red) spheres. (c) Calculated variation of the total energy (relative to the energy of the initial configuration) for the bond breaking reaction path (from (a) to (b)), for different compression strains: 0.459 (red), 0.465 (blue), 0.471 (green). The corresponding energy ΔE as a function of strain for the transition (a)$\longrightarrow$(b) is reported in the inset graph. The extrapolation of this curve suggests that the energy barrier vanishes for $\varepsilon \simeq 0.476$.

Our calculations reveal that the compression of C_{60} can be analyzed according to three strain domains. For strain values lower than 0.47–0.50, the deformation is purely elastic i.e., a perfect molecule is recovered when the load is removed. For larger strains, but still lower than 0.73–0.76, bond breaking events occur in the equatorial region of the molecule. However partial or total structure recovery can be obtained, with a significant influence of unloading conditions. Finally, for strains greater than 0.73–0.76, the structural damages become severe enough to prevent any recovery. We favor the use of contact force rather than energy to determine these strain thresholds. In fact, a thorough analysis of many simulations reveals that the energy drops visible in Figs. 2 or 5 are mostly due to stochastic bond reconstruction events, occurring at higher strains than the first bond breaking. Therefore the contact force is a better quantity than energy to determine the onset of C_{60} shell failure.

With this criterion, the first strain threshold ranges from 0.47 to 0.50, taking into account all calculations. There is an intrinsic uncertainty associated with the determination of the strain for such a small system. Furthermore we find that critical strain values depend on the compression orientation, and also on temperature (Fig. 6). This thermal dependence indicates that the first bond breaking event is also a stochastic event. A critical issue is therefore the possible influence on our results of the high strain rate used in molecular dynamics simulations. Theoretical analysis indeed show that a lowering of the computed elas-

tic limit and of the critical stress is expected when extrapolating to typical experimental strain rates [42, 43]. To tackle this issue we performed NEB calculations of the activation energy for the first bond breaking event in the case of a H orientated molecule. An initial reaction path was built between a perfect C_{60} structure and another where a C–C bond was broken (Fig. 12-(a-b)), both configurations being relaxed and for several compression strains. The results of the NEB calculations are represented in Fig. 12-(c). As expected, the activation energy ΔE is low and strongly dependent on the compression strain. In fact, it is equal to 0.218 eV for a strain of 0.459, and extrapolation of the data shows that the barrier vanishes for a strain close to 0.476. Our calculations also reveal that the bond broken C_{60} structure (Fig. 12-(b)) becomes unstable at a compression strain of 0.453, the C–C bond reforming during relaxation. This defines an absolute minimum value for the critical strain at which the first bond breaking event occurs. The thermal activation of this mechanism is therefore only possible in the strain range 0.453–0.476. This suggests that the influence of the strain rate used in MD calculations is very limited, with an overestimation of the elastic limit of at most 2%.

Quantitative information on the onset of C_{60} shell failure is scarce in literature. Available studies rely on empirical potentials description and do not provide explicit critical strains [10, 11, 40]. Our own investigations revealed that different potentials all overestimate the elastic limit, with values greater than 0.60 [19]. However, a recent work by Seo and Kim suggests that the first bond breaking event occurs for a C_{60} height of about 4.5 Å i.e., a critical strain of 0.35 [40]. The cause for such a disagreement with the present study and published works is unclear.

The second important result to discuss is the partial or full recovery of the defected C_{60}, with an appreciable influence of the unloading conditions. This regime is defined by compression strains between 0.48 ± 0.02 and 0.75 ± 0.02, where the C_{60} energy is in the range 40–80 eV. The various bond breaking events occurring in this regime are associated with energy drops of 4 eV on average (with extreme values of 1 eV and 9 eV), computed from all our simulations. This value has to be compared to the maximum potential energy reached during compression, that is 82 eV on average. Only a small fraction of this energy is released by the first bond breaking events, and the remaining part is stored as an elastic energy in the molecule. In F unloading simulations, this energy is quickly converted into kinetic energy and the fast uniaxial expansion of the molecule helps to heal the defects created during the compression, leading to full recovery in several cases. In contrast, in S unloading simulations the stored elastic energy is essentially converted to thermal energy, and lost by exchange with the thermostat. Full recovery in these conditions only happens when C_{60} shell openings are not reconstructed.

S simulations can be compared to the unloading stage in a nanoindentation experiment. Usual strain rates of 10^{-1}–10^{-3} s^{-1} imply that the sample is always at thermal equilibrium. This is reproduced in the simulations by the use of a ionic thermostat. Conversely F unloading simulations are comparable to experiments where fullerenes with high kinetic energy are colliding with materials surfaces [3]. The C_{60} molecule is observed to rebound with no fragmentation for a defined energy range. Pionering simulations showed that the C_{60} molecule is first flattened, then leaves the surface with a certain speed [4, 5]. The release process is equivalent to our F unloading simulations. However only a qualitative comparison can be made, since in experiments a non negligible part of the incoming molecule energy is dissipated by interacting with the substrate. Also, the elastic discharge of the latter is likely to impact the release velocity. Nevertheless, our results suggest that most rebounding molecules are not perfect and include structural defects, in agreement with the early study by Galli and Mauri [5]. Furthermore, they also mention that a significant proportion of these molecules could be free of any defects.

Finally, it is worth emphasizing that C_{60} was described as a *resilient* molecule in these pioneering experiments, due to its ability to 'survive' these high energy collisions. In materials science resilience is formally defined as the ability of a material to withstand elastic deformation without deforming plastically, and it is usually expressed as an energy per volume. For instance, the resiliences of steel and carbon fibers are approximately 6 MJ m^{-3} and 25 MJ m^{-3}, while for spider silk it can be as large as 180 MJ m^{-3} [44]. Our study shows that an elastic behavior is always obtained for compression strains lower than 0.48 ± 0.02, with a maximum elastic energy of 40 eV on average. Assuming that the diameter of C_{60} is approximately 7 Å, this energy corresponds to an extraordinary resilience of 36×10^3 MJ m^{-3} i.e., 200 times higher than for spider silk.

5. Conclusions

Density functional theory molecular dynamics calculations have been carried out to determine the mechanical properties of the buckminsterfullerene C_{60} at finite temperature and with first-principles accuracy. In particular, we focus on the compression of the molecule as well as on two different unloading modes. These calculations lead to several original findings, which further illustrate the unique features of C_{60}. Hence three different domains can be defined depending on the compression strain. In the first one, for strain values below 0.48 ± 0.02, the deformation is exclusively elastic. It is shown that the stiffness and the electronic gap depend on the molecule orientation with respect to the compression. Second, in the domain defined by strains between 0.48 ± 0.02 and 0.75 ± 0.02, C–C bond breaking events occur in the equatorial region with a clear stochastic character. This onset of C_{60} shell rupture is associated with a contact force plateau of 30–32 nN regardless of temperature or compression orientation. A surprising finding is the possible recovery of the

C_{60} shell structural integrity after unloading. This is especially true for fast unloading which yields a significant proportion of fully recovered molecules, or with low energy defects, compared to a slow unloading. This dynamical recovery phenomenon might be explained by the high stored elastic energy compared to the energy associated with C_{60} shell breaking events. Finally, for strains greater than 0.75 ± 0.02, the C_{60} shell damaging reaches a point of no return, with no possible recovery by unloading. The existence of three strain regimes is unusual, and further emphasizes the uniqueness of fullerenes compared to other nanostructures [45].

Finally, our study is based on first principles calculations which are more accurate and reliable than empirical potentials. This is especially true in situations of large deformations as encountered here. Another advantage of first principles calculations is that including different chemical species is straightforward. A natural extension of the present work is therefore to investigate the influence on mechanical properties of endohedral inclusions like noble gas atoms or small molecules in fullerenes. Works are currently in progress in these directions. One could also mention the potential application of the present method to ordered C_{60} thin films. A recent study suggests that compression simulations lead to similar results for a single molecule and a thin film, at low and moderate strains [40]. It would then be interesting to carry out first-principles MD calculations for further confirmation.

Acknowledgements

Computer time for this study was provided by several computing facilities: the Spin Center at the University of Poitiers, the MCIA (Mésocentre de Calcul Intensif Aquitain), and GENCI-CINES (Grant 2020-A0090912035). We also acknowledge support by the French government program "Investissements d'Avenir" (EUR INTREE, reference ANR-18-EURE-0010).

Declaration of competing interest

The author declares that he has no known competing financial interests or personal relationships that could have appeared to influence the work reported in this paper.

References

[1] M. Dresselhaus, G. Dresselhaus, P. Eklund, Science of Fullerenes and Carbon Nanotubes, Academic Press, San Diego, 1996.

[2] W. Andreoni (Ed.), The Physics of Fullerene-Based and Fullerene-Related Materials, Springer Netherlands, 2000. doi:10.1007/978-94-011-4038-6.

[3] R. D. Beck, P. S. John, M. M. Alvarez, F. Diederich, R. L. Whetten, Resilience of all-carbon molecules c_{60}, c_{70}, and c_{84}: a surface-scattering time-of-flight investigation, J. Phys. Chem. 95 (21) (1991) 8402–8409. doi:10.1021/j100174a066.

[4] R. Mowrey, D. Brenner, B. Dunlap, J. Mintmire, C. White, Simulations of c_{60} collisions with a hydrogen-terminated diamond (111) surface, J. Phys. Chem. 95 (1991) 7138–7142.

[5] G. Galli, F. Mauri, Large scale quantum simulations: C_{60} impacts on a semiconducting surface, Phys. Rev. Lett. 73 (25) (1994) 3471–3474. doi:10.1103/physrevlett.73.3471.

[6] Z. Pan, J. Xie, Z. Man, Simulations of c_{60} in collision with diamond surfaces, Nucl. Instrum. Meth. Phys. Res. B 135 (1-4) (1998) 346–349. doi:10.1016/s0168-583x(97)00609-5.

[7] S. Woo, S. H. Lee, E. Kim, K. Lee, Y. H. Lee, S. Y. Hwang, I. C. Jeon, Bulk modulus of the c60 molecule via the tight binding method, Phys. Lett. A 162 (6) (1992) 501–505. doi:10.1016/0375-9601(92)90014-d.

[8] J. Cai, R. Bie, X. Tan, C. Lu, Application of the tight-binding method to the elastic modulus of c60 and carbon nanotube, Physica B 344 (1-4) (2004) 99–102. doi:10.1016/j.physb.2003.10.003.

[9] E. Ghavanloo, R. Izadi, A. Nayebi, Computational modeling of the effective young's modulus values of fullerene molecules: a combined molecular dynamics simulation and continuum shell model, J. Mol. Modeling 24 (71) (2018) 1–7. doi:10.1007/s00894-018-3623-x.

[10] D. Brenner, J. Harrison, C. White, R. Colton, Molecular dynamics simulations of the nanometer-scale mechanical properties of compressed buckminsterfullerene, Thin Solid Films 206 (1-2) (1991) 220–223. doi:10.1016/0040-6090(91)90425-w.

[11] Z. X. Zhang, Z. Y. Pan, Y. X. Wang, Z. J. Li, Q. Wei, Simulations of the nanomechanical properties of compressed small fullerenes, Modern Physics Letters B 17 (16) (2003) 877–884. doi:10.1142/s021798490300586x.

[12] H. Shen, The compressive mechanical properties of cn(n=20, 60, 80, 180) and endohedral m@c60(m=na, al, fe) fullerene molecules, Molecular Physics 105 (17-18) (2007) 2405–2409. doi:10.1080/00268970701679467.

[13] B. I. Yakobson, P. Avouris, Mechanical properties of carbon nanotubes, in: Topics in Applied Physics, Springer Berlin Heidelberg, 2001, pp. 287–327.

[14] V. Harik (Ed.), Trends in Nanoscale Mechanics, Springer Netherlands, 2014. doi:10.1007/978-94-017-9263-9.

[15] S. Hoen, N. G. Chopra, X.-D. Xiang, R. Mostovoy, J. Hou, W. A. Vareka, A. Zettl, Elastic properties of a van der waals solid:c60, Phys. Rev. B 46 (19) (1992) 12737–12739. doi:10.1103/physrevb.46.12737.

[16] A. Matsumuro, Y. Takada, Y. Takahashi, I. Kondo, M. Senoo, Mechanical properties of c_{60} bulk materials synthesized at high pressure, Rev. High Pressure Sci. Technology 7 (1998) 823–825.

[17] W. Qiu, S. Chowdhury, R. Hammer, N. Velisavljevic, P. Baker, Y. K. Vohra, Physical and mechanical properties of c60under high pressures and high temperatures, High Press. Res. 26 (3) (2006) 175–183. doi:10.1080/08957950600834792.

[18] Y. Funamori, R. Suzuki, T. Wakahara, T. Ohmura, E. Nakagawa, M. Tachibana, Large elastic deformation of c_{60} nanowhiskers, Carbon 169 (2020) 65–72. doi:10.1016/j.carbon.2020.07.061.

[19] L. Pizzagalli, Finite-temperature mechanical properties of nanostructures with first-principles accuracy, Phys. Rev. B 102 (9) (2020) 094102.

[20] D. Mordehai, S.-W. Lee, B. Backes, D. J. Srolovitz, W. D. Nix, E. Rabkin, Size effect in compression of single-crystal gold microparticles, Acta Mater. 59 (13) (2011) 5202 – 5215. doi:http://dx.doi.org/10.1016/j.actamat.2011.04.057.

[21] L. Hale, D.-B. Zhang, X. Zhou, J. Zimmerman, N. Moody, T. Dumitrica, R. Ballarini, W. Gerberich, Dislocation morphology and nucleation within compressed si nanospheres: A molecular dynamics study, Comp. Mat. Sci. 54 (0) (2012) 280 – 286.

[22] S. Bel Haj Salah, C. Gerard, L. Pizzagalli, Influence of surface atomic structure on the mechanical response of aluminum nanospheres under compression, Comp. Mat. Sci. 129 (2017) 273–278. doi:10.1016/j.commatsci.2016.12.033.

[23] D. Kilymis, C. Gérard, J. Amodeo, U. Waghmare, L. Pizzagalli, Uniaxial compression of silicon nanoparticles: An atom-

istic study on the shape and size effects, Acta Mater. 158 (2018) 155–166. doi:10.1016/j.actamat.2018.07.063.
[24] J. J. Bian, L. Yang, X. R. Niu, G. F. Wang, Orientation-dependent deformation mechanisms of bcc niobium nanoparticles, Philos. Mag. 98 (20) (2018) 1848–1864.
[25] P. Hohenberg, W. Kohn, Inhomogeneous electron gas, Phys. Rev. 136 (3B) (1964) B864–B871.
[26] W. Kohn, L. J. Sham, Self-consistent equations including exchange and correlation effects, Phys. Rev. 140 (4A) (1965) A1133–A1138.
[27] P. Giannozzi, O. Andreussi, T. Brumme, O. Bunau, M. B. Nardelli, M. Calandra et al., Advanced capabilities for materials modelling with quantum ESPRESSO, J. Phys.: Condens. Matter 29 (46) (2017) 465901. doi:10.1088/1361-648x/aa8f79.
[28] J. P. Perdew, K. Burke, M. Ernzerhof, Generalized gradient approximation made simple, Phys. Rev. Lett. 77 (18) (1996) 3865–3868.
[29] D. Vanderbilt, Soft self-consistent pseudopotentials in a generalized eigenvalue formalism, Phys. Rev. B 41 (11) (1990) 7892–7895.
[30] B. P. Feuston, W. Andreoni, M. Parrinello, E. Clementi, Electronic and vibrational properties of c_60 at finite temperature from ab initio molecular dynamics, Phys. Rev. B 44 (8) (1991) 4056–4059. doi:10.1103/physrevb.44.4056.
[31] C. S. Yannoni, P. P. Bernier, D. S. Bethune, G. Meijer, J. R. Salem, Nmr determination of the bond lengths in c_{60}, Journal of the American Chemical Society 113 (8) (1991) 3190–3192. doi:10.1021/ja00008a068.
[32] F. Tassone, F. Mauri, R. Car, Acceleration schemes for *ab initio* molecular-dynamics simulations and electronic-structures calculations, Phys. Rev. B 50 (15) (1994) 10561–10573.
[33] H. Jónsson, G. Mills, K. W. Jacobsen, Nudged elastic band method for finding minimum energy paths of transitions, in: B. J. Berne, G. Ciccotti, D. F. Coker (Eds.), Classical and Quantum Dynamics in Condensed Phase Simulations, World Scientific, 1998, Ch. 16, p. 385.
[34] G. Henkelman, B. P. Uberuaga, H. Jónsson, A climbing image nudged elastic band method for finding saddle points and minimum energy paths, J. Chem. Phys. 113 (22) (2000) 9901–9904.
[35] P. Mahler Larsen, S. Schmidt, J. Schiøtz, Robust structural identification via polyhedral template matching, Modelling Simul. Mater. Sci. Eng. 24 (5) (2016) 055007. doi:10.1088/0965-0393/24/5/055007.
[36] Z. Wang, K. Su, H. Fan, L. Hu, X. Wang, Y. Li, Z. Wen, Mechanical and electronic properties of c_{60} under structure distortion studied with density functional theory, Comp. Mat. Sci. 40 (4) (2007) 537–547. doi:10.1016/j.commatsci.2007.02.003.
[37] R. Pawlak, S. Kawai, S. Fremy, T. Glatzel, E. Meyer, Atomic-scale mechanical properties of orientated c_{60} molecules revealed by noncontact atomic force microscopy, ACS Nano 5 (8) (2011) 6349–6354. doi:10.1021/nn201462g.
[38] C. Joachim, J. K. Gimzewski, R. R. Schlittler, C. Chavy, Electronic transparence of a single c_{60} molecule, Phys. Rev. Lett. 74 (11) (1995) 2102–2105.
[39] M. Lantz, S. O'Shea, M. Welland, Measurement of forces during the modification of c60 islands, Surf. Sci. 437 (1-2) (1999) 99–106. doi:10.1016/s0039-6028(99)00698-6.
[40] K.-J. Seo, D.-E. Kim, Molecular dynamics investigation on the nano-mechanical behaviour of c60 fullerene and its crystallized structure, Nanoscale 12 (2020) 9849–9858.
[41] J. Menéndez, J. Page, Vibrational spectroscopy of c_{60}, in: M. Cardona, G. Güntherodt (Eds.), Light Scattering in Solids VIII, Springer, Berlin, 2000.
[42] J. Li, The mechanics and physics of defect nucleation, Mater. Res. Soc. Bull. 32 (2007) 151–159.
[43] T. Zhu, J. Li, A. Samanta, A. Leach, K. Gall, Temperature and strain-rate dependence of surface dislocation nucleation, Phys. Rev. Lett. 100 (025502) (2008) 1–4.
[44] L. Römer, T. Scheibel, The elaborate structure of spider silk, Prion 2 (4) (2008) 154–161. doi:10.4161/pri.2.4.7490.
[45] J. Amodeo, L. Pizzagalli, Modeling the mechanical properties of nanoparticles: a review, Comptes Rendus Physique 22 (S3) (2021) 1–32. doi:10.5802/crphys.70.